Earth and Planetary Science Letters 275 (2008) 246–257

Contents lists available at ScienceDirect

Earth and Planetary Science Letters

journal homepage: www.elsevier.com/locate/epsl

# Measurement of interseismic strain across the Haiyuan fault (Gansu, China), by InSAR

O. Cavalié [a,*,1], C. Lasserre [a,1], M.-P. Doin [a], G. Peltzer [b,c], J. Sun [d], X. Xu [d], Z.-K. Shen [b]

[a] Laboratoire de Géologie, École Normale Supérieure, CNRS, 24 rue Lhomond, 75231 Paris Cedex 05, France
[b] Department of Earth and Space Sciences, University of California, 595 Charles Young Drive East, Los Angeles, CA 90025-1567, USA
[c] Jet Propulsion Laboratory, California Institute of Technology, Pasadena, California, USA
[d] Institute of Geology, Chinese Earthquake Administration, PO Box 9803, Beijing 100029, China

ARTICLE INFO

*Article history:*
Received 4 January 2008
Received in revised form 25 July 2008
Accepted 29 July 2008
Available online 2 October 2008

Editor: C.P. Jaupart

*Keywords:*
InSAR
active tectonics
fault creep
interseismic deformation
atmospheric phase propagation delays
Haiyuan fault
Asia

ABSTRACT

The Haiyuan fault is part of a major left-lateral fault system at the northeastern edge of the Tibet-Qinghai plateau. Two M8 earthquakes (1920 and 1927) occurred along the fault, bracketing an unbroken section of the fault identified as the Tianzhu seismic gap. We use interferometric synthetic aperture radar data from descending orbits of the ERS satellites, acquired between 1993 and 1998 along two adjacent tracks covering the gap, to measure the current surface movements and better understand the present day mechanical behavior of this fault section. The analysis of the radar data involves first the combined correction of orbital errors and errors associated with the phase delay through the troposphere. A subset of the data is then selected based on the analysis of the residual noise spectra for each pair of data. The selected interferograms are stacked and the average phase change rate is converted in fault-parallel velocity assuming that the ground movement is horizontal and parallel to the fault. Velocity maps from both tracks show a zone of high velocity gradient across the fault, a few kilometers wide, consistent with left-lateral slip on the Haiyuan fault. The average velocity field from the two tracks in their overlapping area is well fit with a single screw dislocation model in an elastic half-space. The derived fault slip rate at depth (4.2–8 mm/yr) is consistent with recent GPS results. The corresponding shallow apparent locking depth (0–4.2 km) can be explained by a current low stress accumulation on the fault due to creep almost on the entire fault plane. However, unless it is transient, this creep would be paradoxical with the occurrence of past large earthquakes along this fault section, as revealed by paleoseismology. An alternative model, implying both shallow creep in the brittle upper crust and deep aseismic slip beneath the seismogenic layer, separated by a locked section, would be consistent with InSAR observations and with the potential for large earthquakes on the fault as well. A two-dislocation model with slip at 5 mm/yr beneath 15 km and a transient creep rate of 11 mm/yr between 2 and 7 km fits the InSAR data. However, the width and creep rate of the shallow creeping zone and their possible along-strike variations are still poorly resolved with the present data set.



## 1. Introduction

The continental collision between India and Asia, initiated ~50 Ma ago, is responsible for the deformation of a broad area, including the Himalaya, the Tibetan plateau and Mongolia (e.g., Molnar and Tapponnier, 1975; Tapponnier and Molnar, 1977). In the northern part of the plateau, the deformation is characterized by north-east to east-striking, left-lateral faults, the Altyn Tagh, Kunlun, and Haiyuan faults, combined with SE-striking thrusts in the Qaidam basin and the Qilian Shan (Fig. 1a). Both types of faults contribute to the rising and eastward extrusion of lithospheric blocks (Meyer et al., 1998). However, opposing views exist about their relative role and the proportion of the North–South shortening they accommodate (e.g., Tapponnier et al., 2001; England and Molnar, 2005). A better quantification of the deformation partitioning in this region relies in part on the systematic determination of fault slip rates at geological (late Pleistocene–Holocene) and geodetic (decadal) time scales. The analysis of both long-term and short-term fault behavior is also important for understanding stress loading and slip processes throughout successive seismic cycles, providing insights into seismic hazard. In Tibet, several studies, based on neotectonic observations (Van der Woerd et al., 1997; Mériaux et al., 2004, 2005; Cowgill, 2007) and GPS data (Wang et al., 2001; Shen et al., 2001; Zhang et al., 2004), have provided constraints on fault slip rates. More recently, radar interferometry (InSAR) has also been successfully used to study coseismic (Peltzer et al., 1999; Lasserre et al., 2005; Funning et al., 2007), postseismic (Ryder et al., 2007) and interseismic movements (Wright et al., 2001; Taylor and Peltzer, 2006; Lasserre et al., 2007). The present study contributes to this effort by better documenting the current surface movement along the Haiyuan fault in north-east Tibet.

* Corresponding author.
*E-mail addresses:* cavalieo@ujf-grenoble.fr (O. Cavalié), cecile.lasserre@ujf-grenoble.fr (C. Lasserre), doin@geologie.ens.fr (M.-P. Doin), peltzer@ess.ucla.edu (G. Peltzer).

0012-821X/$ – see front matter © 2008 Elsevier B.V. All rights reserved.
doi:10.1016/j.epsl.2008.07.057

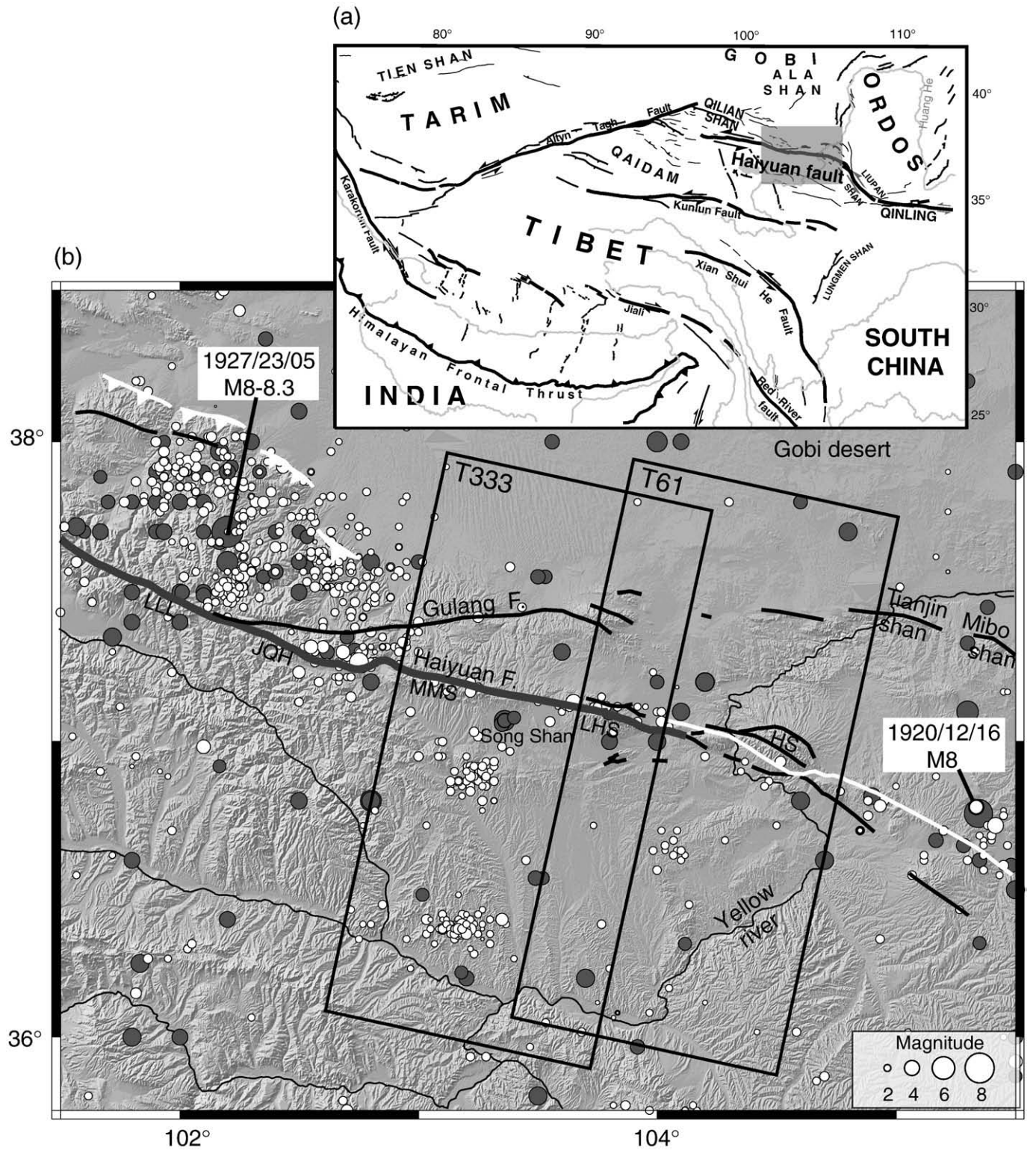


**Fig. 1.** (a) Tectonic map of India–Asia collision zone. Grey box across Haiyuan fault indicates location of Fig. 1b. (b) Seismotectonic map of Haiyuan fault system. Surface ruptures associated with the $M \geq 8$ 1920 and 1927 earthquakes are indicated in white. Tianzhu seismic gap segment (Gaudemer et al., 1995) is outlined in bold grey. Grey circles are $M_W > 4$ earthquakes for the period 1920–1993 and white circles correspond to the $M_W < 5$ for the period 1993–1998 (covered by ERS acquisitions). Compilation is from Lasserre et al. (2001) and the Advanced National Seismic System, ANSS. Black rectangles show the coverage of analysed radar data on tracks 333 and 61. LLL: Leng Long Ling, JQH: Jing Qiang He, MMS: Maomao Shan, and LHS: Lao Hu Shan, HS: Hasi Shan segments.

We focus on the ~1000 km-long Haiyuan fault system, which accommodates the relative motion between Tibet and the Gobi Ala Shan platform, at the northeastern rim of the Tibetan plateau (Fig. 1a). Two large earthquakes have ruptured this fault system during the twentieth century (Fig. 1b): the Mw ~ 8 Haiyuan earthquake in 1920 (Deng et al., 1986; Zhang et al., 1987) and the Ml = 8–8.3 Gulang thrust earthquake in 1927 (Repetti, 1928; Gu et al., 1989). Gaudemer et al. (1995) identified the 260 km-long stretch of the fault extending between these two rupture zones as a seismic gap. Owing to the 1920–1927 sequence of earthquakes, they estimated the gap to be the most likely

site for the next large rupture on the fault. Assessing the seismic potential of the so-called "Tianzhu gap" and its hazard is thus an important goal.

Here, we use ERS InSAR data to map the average interseismic velocity field in the Tianzhu gap area for the period 1993–1998 (Fig. 1). We first present the geological setting of the Haiyuan fault, the available radar data and our strategy of analysis. In the last sections, simple models of a fault embedded in an elastic half-space and the slip distribution with depth they predict on the fault are discussed.

## 2. Seismotectonic setting

The Haiyuan fault is a ~1000 km-long left-lateral fault zone, connecting the Qilian Shan in the west, to the Qinling Shan in the east (Gaudemer et al., 1995) (Fig. 1a). Approximately 220 km of the eastern section of the Haiyuan fault ruptured during the 1920, Mw ~ 8, left-lateral event. To the west, north of the fault, the south-dipping thrusts bounding the northeastern Qilian Shan range front ruptured during the 1927 Gulang earthquake (Fig. 1b). These thrusts, as well as the left-lateral Gulang fault and the Tianjing and Mibo thrust systems, have been interpreted as structures merging at depth with the Haiyuan fault (Gaudemer et al., 1995). The 260-km-long Tianzhu seismic gap identified between the 1920 and 1927 rupture zones can be divided into four segments of similar lengths (Liu-Zeng et al., 2007): from west to east (1) the Leng Long Ling segment (LLL), (2) the Jing Qiang He segment (JQH) separated from (3) the Maomao Shan segment (MMS) by the Tianzhu pull-apart basin, and (4) the Lao Hu Shan segment (LHS) connecting to the western end of the 1920 rupture (Fig. 1b).

Neotectonic studies, carried out along the gap and east of it, show an eastward decrease of the Holocene slip rate of the fault. West of the junction between the Haiyuan and Gulang faults, along the LLL segment, Lasserre et al. (2002) estimated a slip rate of 19 ± 5 mm/yr based on the study of one dated offset lateral moraine. East of the junction, along the MMS segment of the gap, the slip rate, determined by dating offset alluvial terraces, decreases to 12 ± 4 mm/yr due to the slip partitioning between the Haiyuan and the Gulang faults (Lasserre et al., 1999) (Fig. 1b). East of the Yellow river, where the Haiyuan fault splays into parallel strands, the analysis of offset geomorphic features, assumed to date the last glacial maximum, yield a lower bound on the fault slip rate of 8 ± 2 mm/yr (Zhang et al., 1988a,b). The total offset and the age of initiation of the Haiyuan fault have also been derived from observations of offset geological and morphological markers at a larger scale. However strong discrepancies exist between various estimates, which are still a matter of debate. The total offset and age of the fault estimated by Burchfiel et al. (1991) along the 1920 ruptured segment are 15 km and 2 Ma, respectively. The estimates of these quantities by Gaudemer et al. (1995) are 95 km (derived from the sigmoidal shape of the Yellow River across the fault) and 10 Ma. Both studies, however, are consistent with a geological slip rate of ~ 10 mm/yr.

The surface morphology along the Tianzhu gap shows clear evidences of large earthquakes in the past. The smallest river offsets observed along the fault within the gap are of 10 m and have been interpreted as being the displacement associated with the last coseismic rupture (Gaudemer et al., 1995; Lasserre et al., 1999). A recent paleosismological study of two trenches across the Song Shan pull-apart basin, between the MMS and LHS segments (Fig. 1b), identified four large earthquakes in the past 3500–3900 years (Liu-Zeng et al., 2007). The average recurrence interval of about 1000 years inferred from these observations corresponds to the elapsed time since the last large event that occurred during the eleventh or twelfth century, possibly corresponding to the winter 1092 A.D. historical earthquake reported in the seismicity catalogues (Gu et al., 1989; Liu-Zeng et al., 2007). A few smaller events are also detected in the trenches, the most recent one, likely corresponding to the Mw 5.8, 1990 earthquake near Song Shan. However, as the smallest events signature in the sediments tends to be masked by larger events, their occurrence and frequency relative to larger earthquakes are difficult to estimate. The recent seismicity indicates that 6 M ~ 5 earthquakes have occurred in the past 20 years near junctions between the gap segments or in the vicinity of the gap (Fig. 1b; Lasserre et al., 2001).

## 3. ERS InSAR data analysis

### 3.1. ERS data set and interferograms formation

To measure the interseismic deformation in the Haiyuan fault area, we use all SAR data acquired by the ERS satellites between 1993 and 1998 from two adjacent, descending orbits imaging the eastern parts of the Tianzhu seismic gap (tracks T333 and T61, Fig. 1b). The few ERS data acquired after 1998 cannot be used due to Doppler centroid variations. We combine 15 images along T333 and 12 images along T61 into 27 and 22 interferograms, respectively. Most of them have perpendicular baselines smaller than 200 m (Fig. 2), which helps maintain good coherence in the mountainous parts of the scenes. We did not use Envisat SAR data due to the inappropriate temporal and spatial baselines in the archive data.

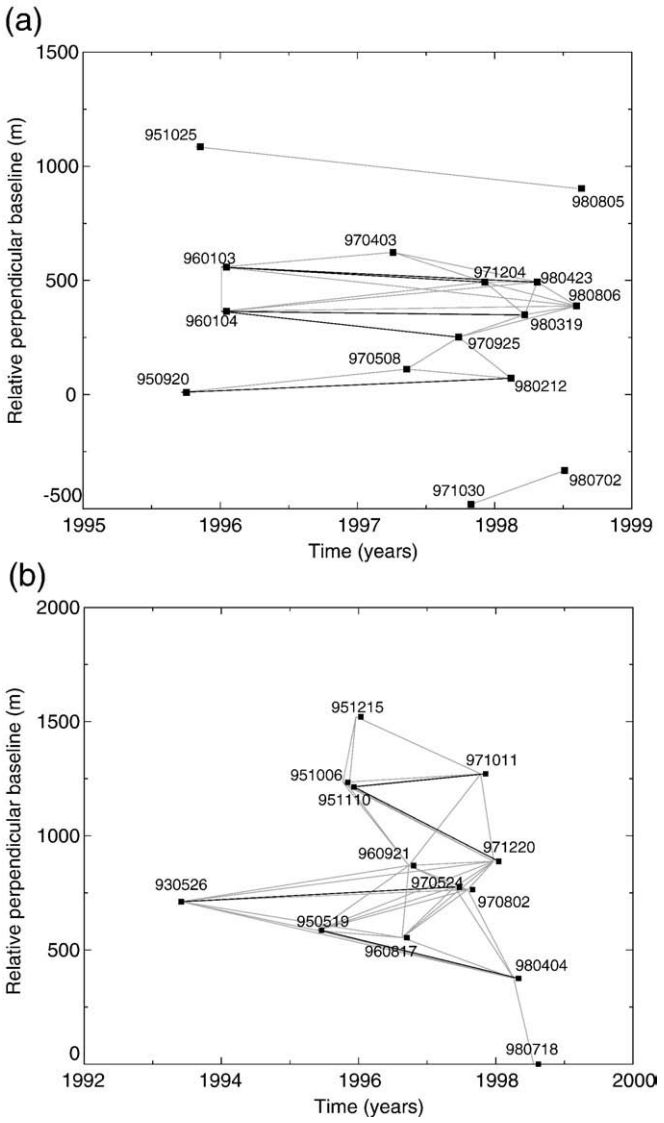


**Fig. 2.** Relative position of ERS orbits on tracks 333 (a) and 61 (b) plotted as a function of image acquisition dates for ERS orbits. Grey lines show image pairs processed into interferograms. Black lines indicate the subset of interferograms selected for stacking (see discussion in text).

We use the JPL/Caltech ROI-PAC software to process the raw radar signal of image pairs into interferograms (Rosen et al., 2004) and the precise ERS orbits provided by DEOS (Scharroo and Visser, 1998). The topographic phase component is removed using the 3-arc sec SRTM (Shuttle Radar Topography Mission) DEM (Digital Elevation Model) (Farr and Kobrick, 2000), after referencing to the WGS84 ellipsoid. Interferograms are downsampled using 4 looks in range and 20 looks in azimuth and georectified to the DEM (ground pixels are ~90×90 $m^2$).

Fig. 3 shows typical examples of interferograms obtained along both tracks. Phase coherence is good over most of the scene. However, temporal decorrelation due to seasonal ground surface changes and erosion is observed north of the scenes in the sand dunes of the Gobi desert or in the mountainous areas of the Maomao Shan, Laohu Shan, and Hasi Shan (Fig. 1b).

The main problem in estimating interseismic deformation from interferograms is that the tectonic signal is combined in the radar Line Of Sight (LOS) with orbital errors and atmospheric phase delays of similar or even larger amplitude (a few millimeters to centimeters, Zebker et al., 1997; Massonnet and Feigl, 1998), and of comparable spatial wavelengths. This implies trade-offs between the different phase components. In some cases, atmospheric effects resulting in strong phase gradients may even be mistaken with the tectonic signal (Puysségur et al., 2007). In our data set, the interseismic deformation can be clearly observed in only a few interferograms (see the phase gradient across the fault, compatible with left-lateral motion, on Fig. 3a). In many cases, atmospheric effects prevail and have to be corrected to allow further tectonic interpretations. These include:

(1) patterns varying randomly in time and space (named type 1 hereafter) due to atmospheric turbulence (Hanssen, 2001). In particular, we observe small ripples or blobs, that are typically a few kilometers wide (Fig. 3b), large patches (Fig. 3b,c) or atmospheric fronts causing high phase gradients (Fig. 3c). The amplitude of these delays can reach 1 to 2 phase cycles (equivalent to ~3 to 6 cm of apparent range change). We observe that interferograms formed with two images acquired in winter tend to contain less atmospheric signal than those formed with images acquired in the summer (Fig. 3a).

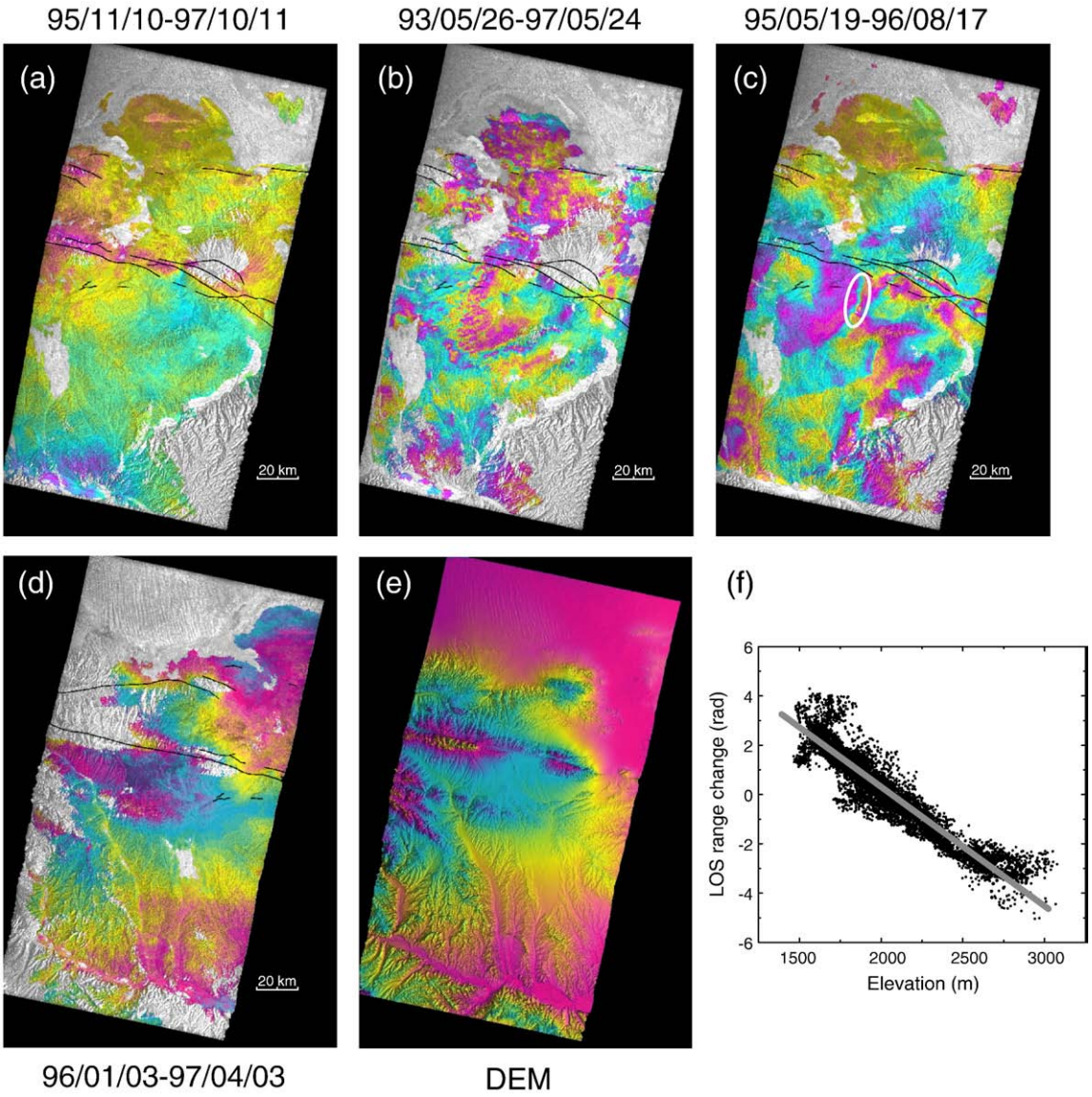


**Fig. 3.** Examples of interferograms, after correction of orbital errors along tracks 61 (a, b, c) and 333 (d). One color cycle (yellow/pink/blue) represents 28 mm of LOS range increase. (e): Scene elevation from SRTM data. One color cycle (yellow/pink/blue) represents 1500 m of elevation decrease. Note patterns of atmospheric delay superimposed on phase change due to fault movement (a), characteristic patterns of atmospheric signal at various spatial scales masking the tectonic signal (b and c) and atmospheric front causing strong phase gradient (white ellipse, c). (f): Phase shown in (d) plotted against scene elevation (e), highlighting correlation between tropostatic delay and elevation. Slope of linear regression line shown in grey is −4.7 rad/km. (For interpretation of the references to colour in this figure legend, the reader is referred to the web version of this article.)

**Table 1**
Summary of the main steps leading to the fault slip and locking depth determination

| |
|---|
| a. Computation of interferograms with baselines lower than 350 m |
| b. For each interferogram: |
| b.1. Estimation of the orbital, tropostatic and displacement terms of Eqs. (1)–(4) |
| b.2. Correction from the orbital and tropostatic terms and referencing |
| c. Interferograms selection based on their signal to noise ratio |
| d. Stack of selected interferograms for both tracks (T333 and T61) independently and in their overlapping area |
| e. Inversion for orbital error, fault-parallel slip rate, and locking depth |

(2) phase delays quasi-linearly correlated with elevation ("tropostatic effect", type 2 hereafter, Fig. 3d to f), resulting mostly from temporal variations of the water vapor, pressure, and temperature stratifications in the troposphere (e.g., Hanssen, 2001). In the Haiyuan fault area, the total water vapor content (TCWV) in the troposphere shows seasonal variations ranging from ~3 mm (+/− a few mm) in winter to ~22 mm (+/− a few tens of mm) in summer (source: European Centre for Medium-Range Weather Forecasts Re-Analysis, ECMWF ERA-40, Uppala et al., 2005). Hence, the tropostatic phase delays ($\varphi_{tropo}$) affecting an interferogram, proportional to ΔTCWV, the TCWV difference between the acquisition times of the two images forming the interferogram ($\varphi_{tropo} \sim \Delta TCWV \times \Pi^{-1}$ with $\Pi \sim 0.15$, Bevis et al., 1992), can reach up to several centimeters, far above the expected tectonic signal.

Data stacking is a common solution to mitigate errors due to atmospheric delays (Zebker et al., 1997), but it requires a large quantity of data. In the next sections, we show that by estimating a first order correction of the tropostatic phase delay and using a careful data selection based on the phase noise, the Signal to Noise Ratio (SNR) of the data stack can be significantly improved, allowing us to retrieve the tectonic signal. All the processing steps described below are summarized in Table 1.

### 3.2. Orbital and atmospheric corrections

The observed interferometric phase difference $\varphi$ can be written as the sum of four terms:

$$\varphi = \varphi_{def} + \varphi_{orb} + \varphi_{tropo} + \varphi_{noise} \quad (1)$$

where $\varphi_{def}$ is the phase component related to tectonic movements, $\varphi_{orb}$ is the residual orbital phase, $\varphi_{tropo}$ is the atmospheric phase delay correlated with elevation and $\varphi_{noise}$ is the random noise due to

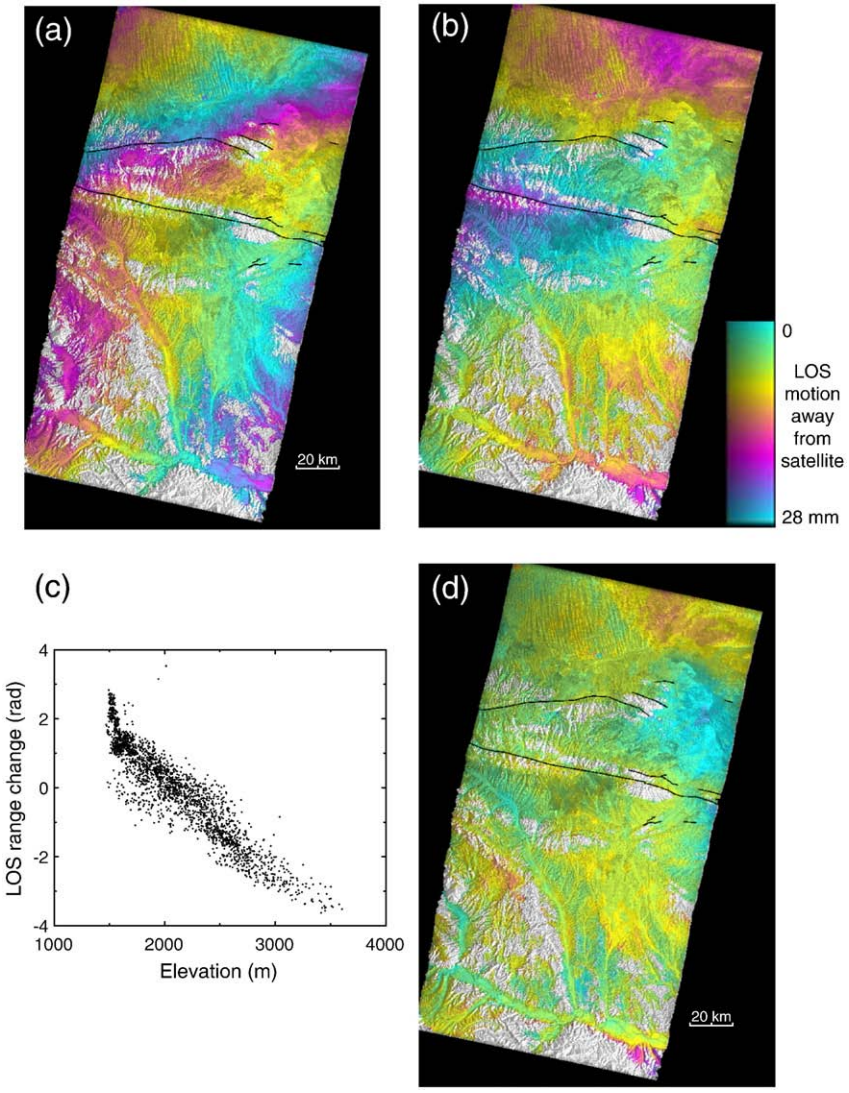


**Fig. 4.** ERS1–ERS2 tandem interferogram (96/01/03–96/01/04) at different steps of post-processing: (a) raw interferogram, (b) after correction from orbital error (see details in text). It displays a phase-elevation correlation shown in (c) with a correlation coefficient $r=-0.92$. (d) Interferogram in (b) after correction from a linear phase-elevation relation. Residual patterns correspond to random atmospheric delays (during the day that separates the two images, no tectonic signal is expected).

turbulent atmospheric delays, as well as instrument noise and temporal decorrelation.

Let us consider a model of surface velocity near a vertical infinite strike–slip fault embedded in an elastic half-space, slipping at depth below a locked crust section of thickness $D_c$. The associated phase change $\varphi_{def}$ can be written as (Savage and Burford, 1973):

$$\varphi_{def}(y') = \frac{4\pi}{\lambda}\left(\sin(i)\cos(\alpha) \times \frac{s}{\pi}\tan^{-1}(y'/D_c)\right), \quad (2)$$

where $y'$ is the distance from the fault along azimuth, $s$ is the displacement on the fault below depth $D_c$ during time interval covered by the interferogram, $i$ is the incidence angle of the radar Line Of Sight (LOS), $\lambda$ is the ERS radar wavelength ($\lambda$=0.0566 m), and $\alpha$ is the angle between fault and direction perpendicular to satellite path. As the azimuth of the Haiyuan fault is close to the direction perpendicular to the satellite orbit, we consider that cos $\alpha \sim 1$.

The residual orbital error, $\varphi_{orb}$, can be expressed as:

$$\varphi_{orb} = (ax + b)y + cx + d, \quad (3)$$

where $x$ and $y$ are pixels coordinates in range and azimuth, respectively (Cavalié et al., 2007). Because of the relative orientation of the fault with respect to the satellite track, both $\varphi_{orb}$ and $\varphi_{def}$ have similar, large wavelength signatures along azimuth. Therefore, the estimates of the orbital ramp in azimuth (parameters a and b in Eq. (3)) and of deformation parameters ($D_c$ and $s$ in Eq. (2)) are correlated in the inversion.

The phase delay related to the tropostatic effect, $\varphi_{tropo}$ (type 2, Section 3.1), is not random in space and correlates with the topography (Hanssen, 2001). Similar studies in Tibet have shown that, in some cases, $\varphi_{tropo}$ (thus the interferometric phase) decreases exponentially (Peltzer et al., 2006) or linearly with elevation (Taylor and Peltzer, 2006). A systematic analysis of all our interferograms shows that the phase-elevation relation is well approximated by a linear function, within the elevation range (1500 m–3500 m) of our study area (Fig. 3). The tropostatic delay, $\varphi_{tropo}$, can thus be modeled as:

$$\varphi_{tropo} = kz, \quad (4)$$

where $z$ is the elevation and $k$ a constant across scene. Such a linear relation is well defined for all interferograms on track 333, as the turbulent component of the atmospheric delay (type 1, Section 3.1) is small. Phase-elevation correlation coefficients are larger than 0.7

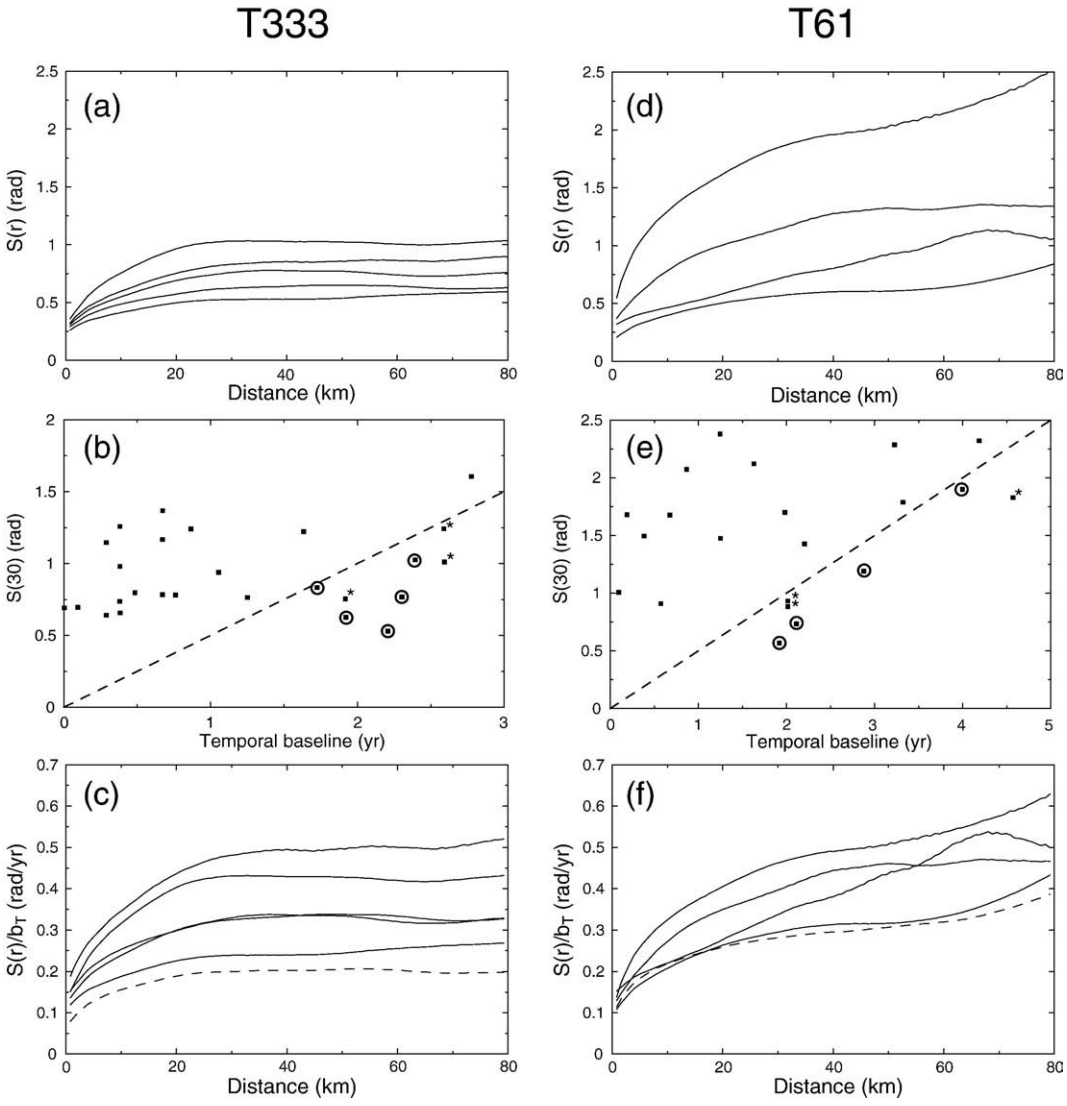


**Fig. 5.** (a) Noise energy function $S(r)$ (see definition in text) of corrected interferograms used in stack of track 333. (b) $S(r=30$ km) for each interferogram of track 333 plotted versus temporal baseline (black squares). Dashed line corresponds to a signal to noise ratio equal to one for a left-lateral slip rate of 6 mm/yr (0.5 LOS rad/yr). Circled squares show interferograms on track 333 selected for stacking (with SNR>1). Squares with star indicate other interferograms with SNR>1 but redundant with other selected interferograms (same images used) and excluded from stack. (c) Same energy functions as in (a) normalized by temporal baselines, $b_T$ (solid lines). Dashed line: energy function of final stack on track 333, built with the subset of interferograms circled shown in (b). (d), (e), (f): same as (a), (b), (c), respectively, for track 61.

for 55% of the interferograms on track 333 and only 10% of the interferograms on track 61.

Finally, $\varphi_{noise}$ includes other sources of noise such as random atmospheric delays (type 1, 3.1), decorrelation noise due to the variability in scattering properties of the surface, instrument noise and coregistration errors. $\varphi_{noise}$ is considered as random in space and time and can be reduced by stacking several independent interferograms (Zebker et al., 1997).

In contrast with the turbulent atmospheric phase screen (random in time and space), a significant residual $\varphi_{tropo}$ term (not random in space, and seasonally dependent) may remain on a stack of interferograms if the distribution of interferograms with positive and negative phase-elevation correlation is unbalanced in the data set (Cavalié et al., 2007). While interferograms on track 61 have equally distributed positive or negative correlation coefficients, 24 out of 27 interferograms on track 333 have a negative phase-elevation correlation. In this latter case, tropostatic delay corrections are necessary. Similarly, residual orbital errors, $\varphi_{orb}$, may not cancel in the stack in the case of a limited data set, and should therefore be estimated and corrected before geophysical interpretation.

The estimation and correction of $\varphi_{orb}$ and $\varphi_{tropo}$ can be done either on the stack or on individual interferograms before stacking. Because both $\varphi_{orb}$ and $\varphi_{tropo}$ add linearly when stacking InSAR data, both options should theoretically give the same results. However, the phase coherence and the unwrapped areas vary significantly from one interferogram to another, depending on the temporal and perpendicular baselines. Therefore, different pixels in a stack correspond to various combinations of interferograms, thus to various orbital ramps ($\varphi_{orb}$) and tropostatic effects ($\varphi_{tropo}$) combinations. We thus choose to correct and reference (averaging the phase to zero) each interferogram independently before stacking (see details in Supplementary Material).

As the orbital ramp cannot be estimated independently from the deformation (trade-off between $\varphi_{orb}$ and $\varphi_{def}$), we choose to jointly estimate $\varphi_{orb}$, $\varphi_{tropo}$ and $\varphi_{def}$, for each interferogram, before any data stacking (Eq. (1)). Using a least square minimization, we solve for parameters $a$, $b$, $c$, $d$, $k$, and $s$ (Eqs. (2)–(4)), for Dc values varying between 0 and 20 km (step b1, Table 1). Each interferogram is then corrected from $\varphi_{tropo}$ and $\varphi_{orb}$ only, and the average phase of the corrected interferogram is set to zero (step b2, Table 1). At this stage, we obtain different sets of corrected interferograms, each set corresponding to a given $D_c$ value. Fig. 4 shows an example of correction on an ERS1-2 tandem pair interferogram for $D_c$=2 km. Corrected interferograms discussed in the following are for $D_c$=2 km as well. The importance of $\varphi_{tropo}$ and $\varphi_{orb}$ corrections, the influence of

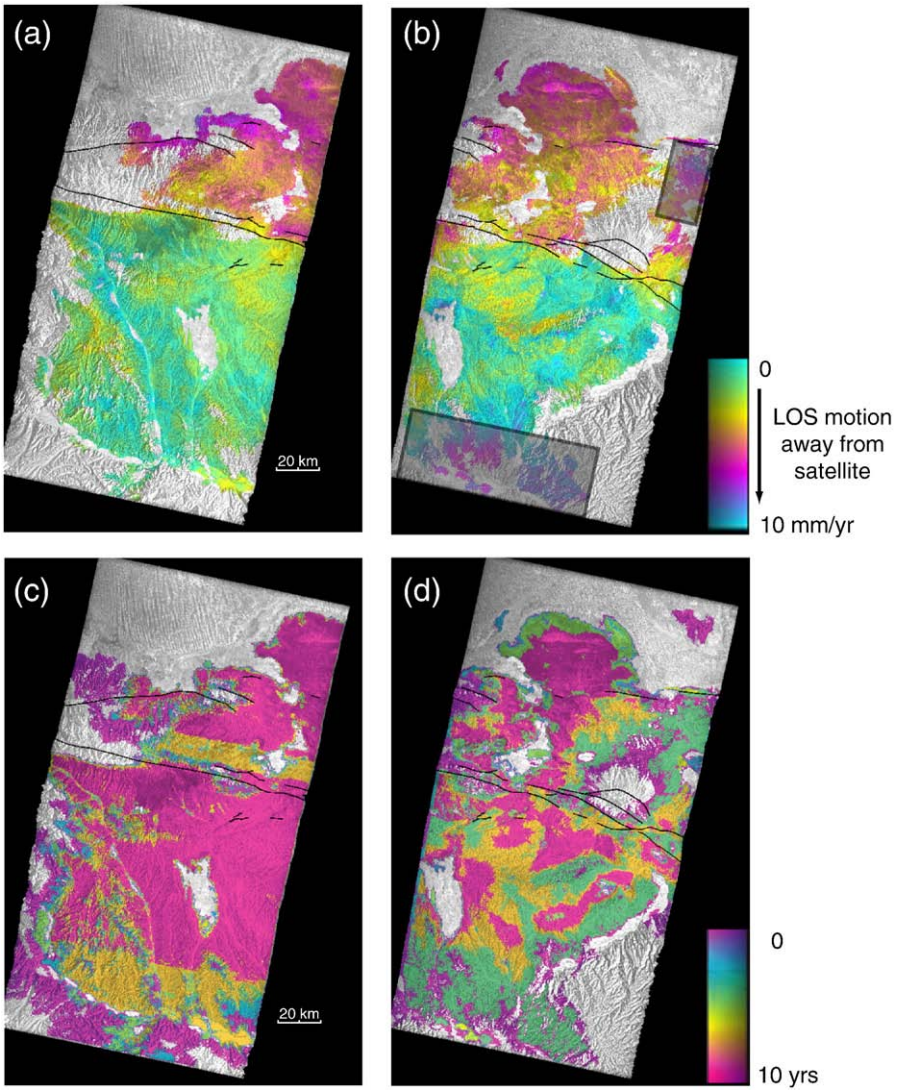


**Fig. 6.** For track 333 (left column) and track 61 (right column): (a) and (b) mean LOS velocity maps, calculated by summing individual selected, unwrapped interferograms (see Fig. 5) and dividing by the cumulative time intervals shown in (c) and (d). Note bands with smaller cumulative time parallel to the radar scanning lines, due to missing lines in one of the scenes used in stack (c). Shaded boxes in (b) outline residual atmospheric noise in areas where only two interferograms are averaged.

performing these corrections before or after data stacking and the little impact of the $D_c$ choice on the final results are discussed in the Supplementary Material.

### 3.3. Interferogram selection

The residual noise in a simple stack of all corrected interferograms (not shown here) is still too large to estimate the deformation rate near the Haiyuan fault. Strong atmospheric delays remain, due to the limited number of independent interferograms and the relatively small cumulative time covered by the stack. Since the residual noise in the stack appears to be dominated by a few images, we select a subset of interferograms based on an evaluation of their SNR.

We first characterize the noise of each interferogram using a function, $S(r)$, which measures the mean absolute phase difference between two pixels separated by the distance $r$ (Puysségur et al., 2007):

$$S(r) = \frac{\sum_{i,j/d(i,j)=r} |\varphi_i - \varphi_j|}{N_r} \quad (5)$$

where $\varphi_i$ and $\varphi_j$ are the interferometric phases of pixels $i$ and $j$, respectively, $d(i, j)$ is the distance separating $i$ and $j$, and $N_r$ is the number of pixel pairs such that $d(i, j)=r$.

To avoid taking into account the phase changes due to the interseismic deformation in the $S(r)$ estimate, the fault area is masked on a 5-km wide band and only the pairs of pixels located on the same side of the fault are considered. After corrections from orbital and tropostatic errors, the $S(r)$ function represents the energy function of the residual noise. For most interferograms, this function increases from $r=0$ to $r\sim30$ km and flattens for greater distances (Fig. 5a,d). 30 km thus corresponds to a characteristic distance above which noise becomes spatially decorrelated. We use $S(30)$ as a proxy to estimate the noise level in each interferogram. Fig. 5b,e show $S(30)$ as a function of the temporal baseline, $b_T$, for each corrected interferogram. The lowest values of $S(30)$ are obtained for interferograms computed with images acquired in winter, when atmospheric noise is low. If the slip rate on the Haiyuan fault is constant, the tectonic signal is proportional to $b_T$ and $b_T/S(30)$ describes the interferogram SNR. The dashed lines on Fig. 5b,e correspond to a SNR equal to 1, assuming a purely left-lateral fault with a rate $s=6$ mm/yr (0.5 rad/yr in radar LOS), which is a reasonable lower bound of the expected slip rate of the Haiyuan fault (Wang et al., 2001). We choose to select for stacking all interferograms combining independent orbits with $\frac{b_T}{S(30)}>2$ yr/rad (SNR>1 under the above assumption). Five interferograms are hence selected on track 333 and four on track 61 (circled squares on Fig. 5b,e and bold lines on Fig. 2).

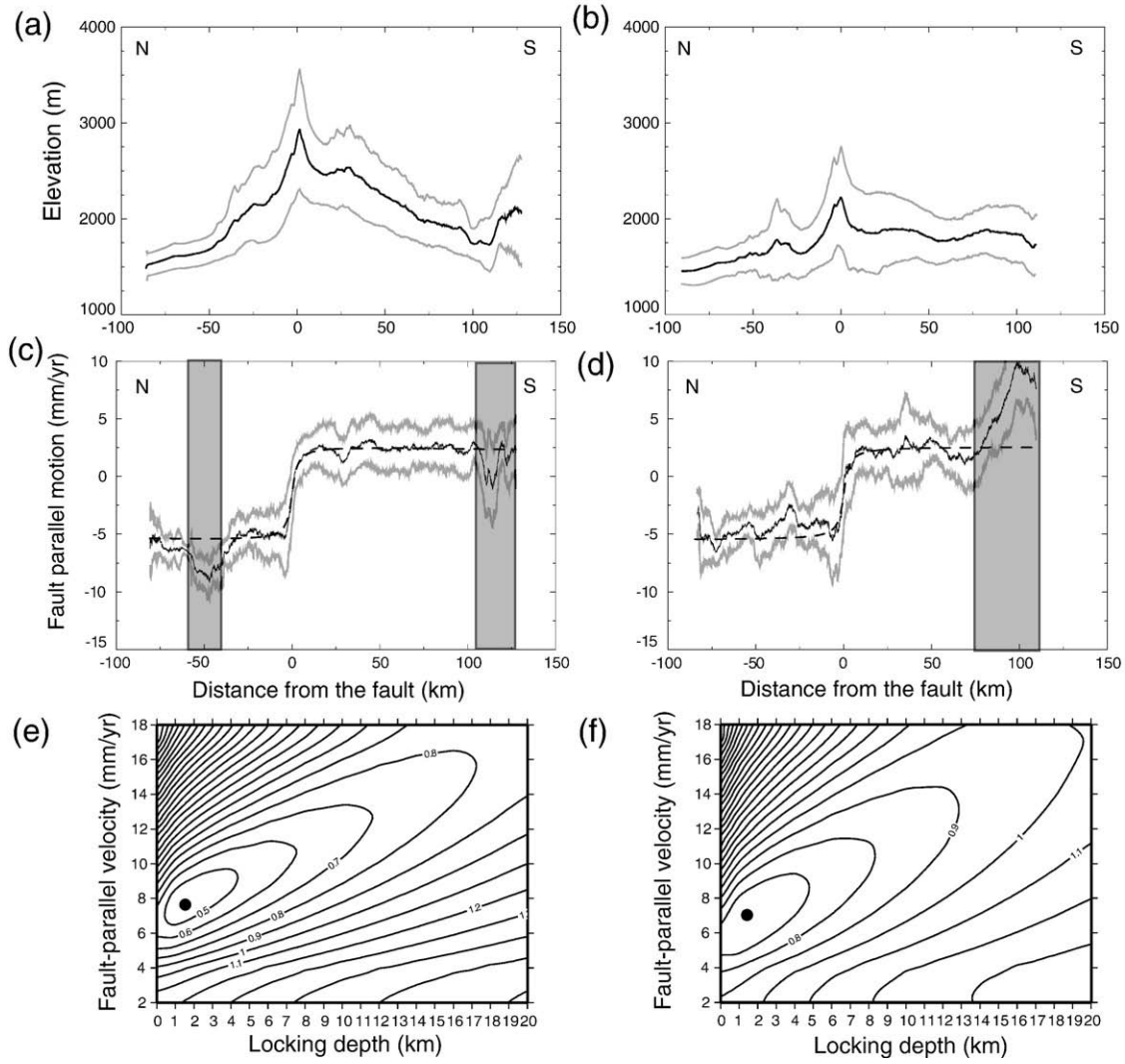


**Fig. 7.** Average fault-perpendicular velocity profiles across ERS scene along track 333 (left column) and 61 (right column): (a) and (b) display the average elevation profiles (black lines) with their standard deviations (grey lines), showing elevation variations along distance perpendicular to profile, (c) and (d) display the fault-parallel velocity profiles (black lines), derived from LOS velocities assuming pure strike–slip motion on the fault. Grey lines are the 1-$\sigma$ lateral velocity deviation from the average profiles. Dashed lines correspond to best fit models in (e) and (f) after excluding the noisiest parts of the profiles (shaded areas). (e) and (f) are the RMS (in mm/yr) misfit between observed and modeled displacements contoured in the model parameter space.

### 3.4. Data stacks: average velocity maps and fault modeling

The average line of sight velocity maps along tracks 333 and 61, obtained by stacking corrected and selected interferograms (Fig. 6a,b), clearly show a steep phase gradient across the Haiyuan fault, consistent with left-lateral shear. This gradient is centered on the LHS segment of the Tianzhu gap west of the Yellow river, then on the fault section which ruptured in 1920 along the HS segment to the east (Figs. 1b and 6a,b), following the active fault traces. The stacks also show a gradual and small LOS velocity change across the Gulang fault, north of the Haiyuan fault. However this signal is not well resolved and might be confused with remaining atmospheric noise. The corresponding maps of cumulative time show more heterogeneities on track 61 than on track 333, due to longer and disparate temporal baselines of interferograms resulting in incomplete phase unwrapping in some scenes (Fig. 6c,d). Overall, although some residual noise remains in places (e.g., Fig. 6b), data corrections, selection, and stacking reduce the noise to an acceptable level, resulting in a flat phase field on each side of the fault.

To estimate a uniform slip rate for the section of the Haiyuan fault comprising the MMS, LHS, and HS segments (Figure 1), we average the observed velocity on a profile perpendicular to the fault, independent for each track. The fault slip is assumed to be purely horizontal, a reasonable assumption, although local vertical motion depending on the fault strike or near segment junctions cannot be totally excluded. The LOS velocities are converted into horizontal, fault-parallel velocities, taking into account the variable line of sight incidence angle between the near range (~19°) and the far range (~27°) of the scene. Only image pixels with a cumulative time larger than 6 years are used to build the mean profiles. The eastern part of track 61 (one third of the scene) is not taken into account due to the complexity of the fault geometry there. The mean profiles for both independent tracks (Fig. 7c,d) show a remarkably consistent velocity step and gradient across the fault. The comparison of the velocity profiles with the average topographic profiles on both tracks (Fig. 7) shows no correlation between the observed signal and the elevation, indicating that the tropostatic component of the phase was successfully removed in the analysis.

To interpret this signal, we first use the conventional fault model applied for the interferogram correction procedure, in which aseismic slip is taking place on a vertical fault plane at a rate $\dot{s}$ beneath a locked crust section of thickness $D$ (Savage and Burford, 1973). The surface displacement rate, $v$, at distance $y$ from the fault is modeled assuming a screw dislocation in an elastic half-space and a residual azimuthal ramp $v_{\mathrm{orb,azi}}$:

$$v = \frac{\dot{s}}{\pi}\tan^{-1}(y/D) + v_{\mathrm{orb,azi}} \quad (6)$$

Note that this equation is the same as that used earlier in the correction step (Section 3.2). We explore the model parameter space over a range of fault slip rates of 2–18 mm/yr and a range of locking depth of 0–20 km. For each locking depth and fault velocity, we find the best fitting ramp in azimuth that minimizes the RMS misfit between the average profile and the model.

Mapping this RMS on a ($\dot{s}$, $D$) plane shows the trade-off between these two parameters (Fig. 7e,f). For both independent tracks the minimum of the misfit is well defined and give remarkably consistent results. It corresponds to a locking depth of ~1.7 km and a slip rate of 7 mm/yr (Fig. 7). The corresponding models are represented by dashed lines on Fig. 7c,d.

We then combine the observed fault-parallel velocity maps from the two tracks in their overlapping area (Figs. 1 and 8). The resulting stack includes 9 interferograms formed with 15 independent radar images and covering a total cumulative time of 20 years. The phase gradient across the fault appears to vary along strike (it is steeper on the eastern part of the LHS segment than on the western one, Fig. 8). However, such variations are still poorly resolved with the current data set. As previously done for each track, we simply compute the average fault-parallel profile on the overlapping area and invert for the fault parameters corresponding to a single dislocation model and an orbital azimuthal ramp. The best fit model, M0, corresponds to a slip rate of 6.3 mm/yr, and a locking depth of 1.7 km (Fig. 9a,b).

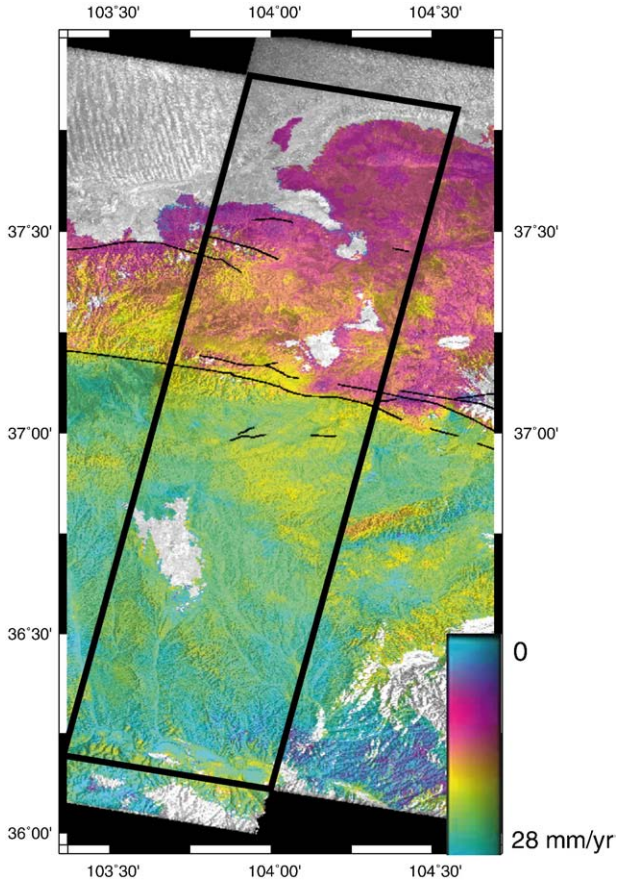


**Fig. 8.** Average fault-parallel velocity map combining tracks 333 and 61 stacks in the overlapping area.

The minimum RMS in the far field (more than 10 km away from the fault) between data and dislocation models with various locking depths is about 0.7 mm/yr (light grey area on Fig. 9b). In the following, we choose this RMS value as representing the average data noise level and use it to limit the domain where the slip rate and the locking depth are confidently estimated. We consider that both the far field data, which constrain the slip rate, and the near field data, which help constrain the fault locking depth, must be fitted to less than this RMS value (Fig. 9b). The ($\dot{s}$, $D$) (dark grey area on Fig. 9b) confidence domain is determined by the intersections of the two 0.7 mm/yr RMS contours, computed using far field and near field data separately (bold lines, Fig. 9b). In this model, the fault-parallel velocity and the locking depth hence range between 4.2 and 8 mm/yr and between 0 and 4.2 km, respectively. GPS measurements (Zhang et al., 2004) are consistent with our InSAR data within their 1-$\sigma$ confidence level (Fig. 9a). However, their inversion seems to indicate a fault slip rate of 5 ±1 mm/yr, lower than the best fit InSAR rate derived above. We show that slightly tilting the InSAR profile in azimuth is sufficient to reconcile InSAR and GPS slip rates (Fig. 9c,d). Model M1 for example, with a misfit to InSAR data smaller than the 0.7 mm/yr RMS bound defined above, has a slip rate estimate of 5 mm/yr, consistent with GPS data (Fig. 9c,d). Note that GPS measurements alone would only give very poor constraints on the locking depth.

## 4. Alternative models and discussion

The InSAR velocity field across the fault is well explained by a single screw dislocation embedded in a homogeneous, elastic half-space. The

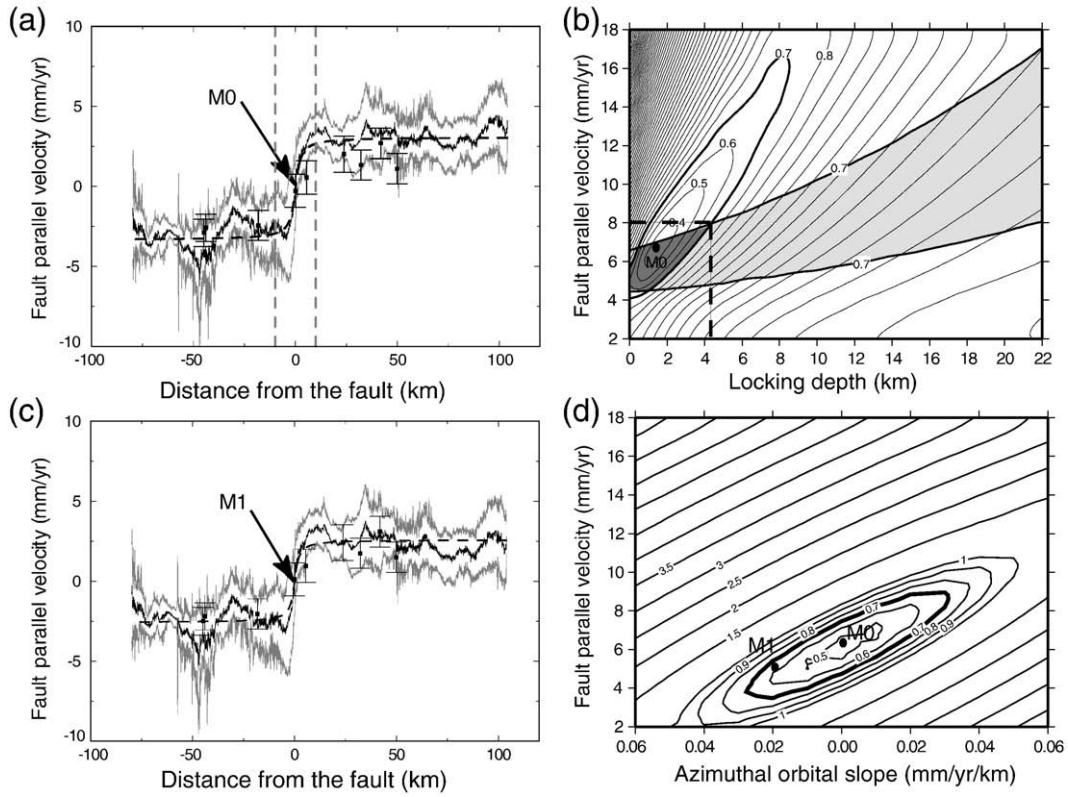


**Fig. 9.** (a) Average fault-parallel velocity profile combining the two stacks in the overlapping part of tracks 333 and 61 (solid black line) with the 1-σ lateral deviation (grey lines). Black dashed line represents model M0, with a locking depth, $D$=1.7 km. Squares represent GPS measurements with associated 1-$\sigma$ errors (Zhang et al., 2004). (b) shows RMS contours in mm/yr (thin lines) for the fault zone delimited by vertical dashed lines in (a), superimposed with the minimum 0.7 mm/yr RMS area for the far field data (light grey area). Dark grey area corresponds to the intersection between the near and far field domains, each delimited by the 0.7 mm/yr RMS contours (see discussion in text). (c) Profile shown in (a) but corrected from a linear ramp to reconcile InSAR and GPS slip rates, corresponding to model M1 with a slip rate of 5 mm/yr and an azimuthal ramp of 0.02 mm/yr/km. Panel (d) shows the RMS contour in the fault-parallel velocity and orbital ramp parameter space, assuming a locking depth of 2 km.

derived fault slip rate at depth (4.2 to 8 mm/yr) is consistent with recent GPS results (Zhang et al., 2004; Cui et al., 2006) (Fig. 9a,c), but lower than Holocene estimates for this section of the Haiyuan fault (12±4 mm/yr, Lasserre et al., 1999). The high velocity gradient near the fault is not the one expected for a fault locked to the bottom of the seismogenic layer and can be the result of (1) a shallow locking depth of the fault, (2) creep at shallow depth on a fault section that is not necessarily connected with the slipping section beneath the seismogenic layer, (3) elastic strain concentration due to a compliant fault zone. We do not consider here more complex viscoelastic earthquake cycle models at this stage.

(1) The hypothesis of long-term, steady creep beneath a shallow locking depth (0–4.2 km) can be ruled out by the evidence of past, large earthquakes in paleoseismology trenches (Liu-Zeng et al., 2007). Moreover, it would be difficult to explain how a fault creeping steadily at depth below 2 km remains locked in the shallowest part of the crust, which is relatively unconsolidated. We therefore do not retain this hypothesis to explain our observations.

(2) The second model involves creep on a shallow patch of the fault that may be disconnected from the steadily slipping section below the seismogenic depth. A few examples of such a behavior have been described for other faults in the world. Creeping segments have been observed along the San Andreas fault (e.g. Scholz et al., 1969), and are surveyed with dense seismometers, GPS and creepmeters networks and InSAR (Johanson and Bürgmann, 2005; Ryder and Bürgmann, submitted for publication). Schmidt et al. (2005) describe shallow creep from the surface to a depth of 4–6 km at a rate of ~5 mm/yr on the Hayward fault in California, using a joint inversion of GPS and InSAR data. Similarly, on the North Anatolian Fault, Turkey, Cakir et al. (2005) show that a segment of the fault is creeping between the surface and a depth of 6 km, using a combined analysis of InSAR and seismological data. In the case of the Haiyuan fault, one can argue that the occurrence of the 1927 earthquake on the Qilian Shan thrusts parallel to and north of the fault (Fig. 1), may have reduced the normal stress on the fault thus reducing friction forces and favoring transient creep at shallow depth. Transients may also occur near the rupture termination of a large event such as the 1920 earthquake, where the shear stress has increased. Interestingly, we note that small seismic events occur in a narrow zone west of the 1920 rupture (in the overlapping area of the studied ERS tracks, Fig. 1). Such events may be driven by variable creep rate along this fault section (Nadeau and McEvilly, 2004). Several other geological observations would support the possibility of creep in the Haiyuan fault area. A large, well-developed gouge zone, ~60 m-wide, has been observed along the fault from the Lao Hu Shan to the eastern bank of the Yellow River (Fig. 1; Lasserre, 2000). Gypsum crystals from Miocene formations trapped in the fault zone are also found, and, south of the Lao Hu Shan, a 500 m-wide shear zone contains serpentinite boudins. Frictional properties of these materials would favor slip on the fault near the surface (Reinen, 2000).

We test a two-dislocation model embedded in an elastic half-space (Savage and Lisowski, 1993) to evaluate the range of depth and rate of a shallow creeping zone permitted by the InSAR data. We align the bottom of the seismogenic layer with the base of the local microseismicity at 15 km (Lasserre, 2000), and impose the slip rate on the deep part of the fault at 5 mm/yr, consistent with GPS data. The shallow creeping section has an upper edge fixed at 1.7 km and we explore the trade-off between the creep rate and

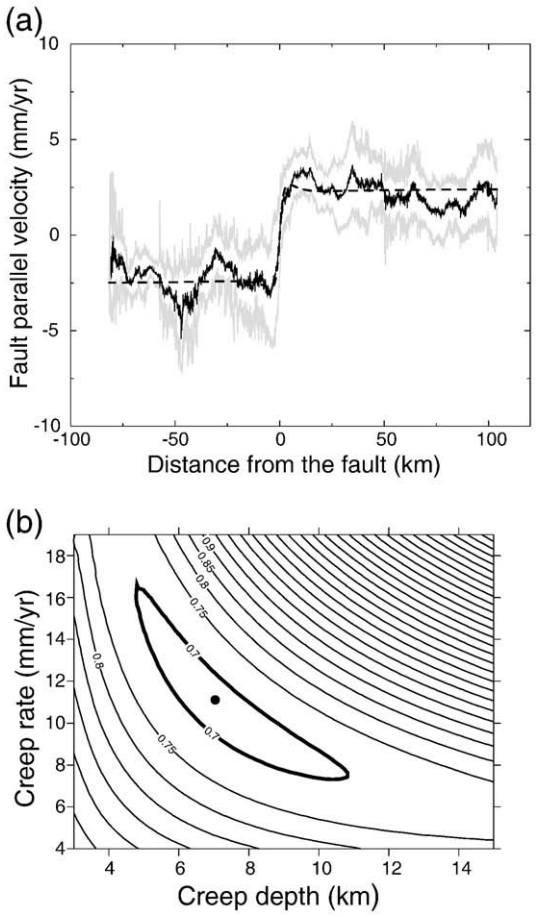


**Fig. 10.** (a) Average fault-parallel velocity profile in the overlapping part of both tracks (solid black line) with the 1-$\sigma$ lateral deviation (grey lines). Black dashed line represents the 2-dislocation model for the best fit parameters (black dot in (b)). (b) shows RMS (in mm/yr) misfit between observed and modeled displacement contoured in the model parameter space.

the bottom edge depth of the creeping zone by fitting the model to the InSAR profile. The best fit is achieved with a creep rate of 11 mm/yr and a bottom edge at 7 km (Fig. 10). The model-data misfit indicates a strong trade-off between these two parameters with a range of 8–16 mm/yr for the creep rate and of 11–5 km for the bottom edge of the creeping zone, with a loosely contrained minimum (Fig. 10b).

The existence of shallow creep does not exclude significant elastic stress to be accumulated on the locked fault section. For example, a recurrence interval of 1000 years between large earthquakes (Liu-Zeng et al., 2007) and a deep slip rate of 5 mm/yr lead to a slip deficit of 5 m on the locked fault section. Considering a mean coseismic displacement of 5 m along a 260 km-long, 8 km-wide segment at depths between 7 km and 15 km, we can compute an equivalent seismic moment $Mo \sim 3.5 \times 10^{20}$ N m (for a shear modulus of 33 GPa). This would correspond, from the relation $\log Mo = 1.5Mw + 9.1$ (Hanks and Kanamori, 1979), to a potential Mw 7.6 earthquake along the Tianzhu gap. Therefore, a two-dislocation model may reconcile the observation of a high velocity gradient near the fault and the occurrence of large earthquakes, confirming that the studied section should still be considered as a seismic gap with high hazard.

(3) Finally, as a third alternative, the simple fact that an extensive damaged zone exists near the modern fault trace could explain the observed concentration of shear in a narrow zone. Compliant fault zones have been identified in other places (e.g. Chen and Freymueller, 2002; Fialko et al., 2002), and are usually explained by a significant reduction of their elastic shear modulus.

## 5. Conclusion

Stacking nine interferograms covering two adjacent tracks allows us to estimate the slip rate of the central section of the Haiyuan fault (~6 mm/yr). The SAR data show a concentration of the surface strain in a narrow zone across the fault, highlighting an interesting behavior of this fault section. The most plausible model to explain the velocity gradient near the fault involves both steady slip at depth beneath the seismogenic zone and transient creep on a shallow part of the fault. This type of behavior is not in contradiction with the occurrence of large earthquake along the fault and does not question the classification of the studied area as a seismic gap. An important trade-off exists between the rate and depth of the possible shallow creep, that cannot be resolved with the present data.

The model results presented here are tested over a single averaged velocity profile perpendicular to the fault. This view of the displacement field may mask lateral variations of the fault creep rate and width, as observed for example along the San Andreas fault (Schmidt et al., 2005; Ryder and Bürgmann, submitted for publication). A better understanding of the Tianzhu fault section behavior would require complementary data. Future analysis of InSAR time series completed with new and frequent Envisat data acquisitions on descending and ascending orbits will help detect possible along-strike variations and determine whether the observed deformation is transient or stable on a decade time scale. Moreover, regular measurements of GPS profiles across the fault will bring stronger constraints on the deep slip rate, which should improve the estimate of the shallow creep properties by InSAR.

It is also important for seismic hazard assessment to know whether the observed deformation style is limited to the seismic gap or not. Studying the segment of the fault which ruptured during the M~8 1920 earthquake to observe possible variations in strain accumulation between a segment that ruptured recently and the Tianzhu gap segment is an important target of future research.

## Acknowledgments

ERS data were provided by the European Space Agency under the Dragon project (ID 2509). This collaborative work was partly funded by the Association Franco-Chinoise pour la Recherche Scientifique et Technique (PRA project T04/04, C. Lasserre and Z.-K. Shen) and the Programme National de Télédétection Spatiale. Gilles Peltzer's contribution was done in part at the Jet Propulsion Laboratory under contract with NASA. We thank two anonymous reviewers, Paul Lundgren, Roland Bürgmann and the associate editor, whose comments greatly improved the manuscript.

## Appendix A. Supplementary data

Supplementary data associated with this article can be found, in the online version, at doi:10.1016/j.epsl.2008.07.057.

## References

Bevis, M.S., Businger, S., Herring, T.A., Rocken, C., Anthes, R.A., Ware, R.H., 1992. Gps meteorology: remote sensing of atmospheric water vapor using the global positioning system. J. Geophys. Res. 74, 253–274.

Burchfiel, B.C., Zhang, P., Wang, Y., Zhang, W., Song, F., Deng, Q., Molnar, P., Royden, L., 1991. Geology of the Haiyuan fault zone, Ningxia-hui autonomous region, China, and its relation to the evolution of the northeastern margin of the Tibetan plateau. Tectonics 10, 1091–1110.

Cakir, Z., Akoglu, A.M., Belabbes, S., Ergintav, S., Meghraoui, M., 2005. Creeping along the Ismetpasa section of the North Anatolian fault (Western Turkey): rate and extent from InSAR. Earth. Planet. Sci. Lett. 238, 225–234.

Cavalié, O., Doin, M.P., Lasserre, C., Briole, P., 2007. Ground motion measurement in the Lake Mead area, Nevada, by differential synthetic aperture radar interferometry

time series analysis: Probing the lithosphere rheological structure. J. Geophys. Res. 112 (B3). doi:10.1029/2006JB004344.
Chen, Q., Freymueller, J.T., 2002. Geodetic evidence for a near-fault compliant zone along the San Andreas fault in the San Francisco bay area. Bull. Seismol. Soc. Am. 92, 656–671.
Cowgill, E., 2007. Impact of riser reconstructions on estimation of secular variation in rates of strike-slip faulting: revisiting the Cherchen River site along the Altyn Tagh Fault, NW China. Earth. Planet. Sci. Lett. 254 (3–4), 239–255.
Cui, D., Wang, Q., Zhang, X., Wang, W., Xu, X., Shenand, Z., Lasserre, C., 2006. Interseismic Deformation of Tianzhu Seismic Gap, Haiyuan Fault, Determined by GPS Observations, Paper Presented at AGU 2006 Western Pacific Geophysics Meeting, Beijing, China, 24–27 July 2006.
Deng, Q., Chen, S., Song, F., Zhu, S., Wang, Y., Zhang, W., Jiao, D., Burchfiel, B., Molnar, P., Royden, L., Zhang, P., 1986. Variations in the geometry and amount of slip on the Haiyuan (Nanxihaushan) fault zone, China, and the surface rupture of the 1920 Haiyuan earthquake. In: Das, S., et al. (Ed.), Earthquake Source Mechanics. Geophys. Monogr. Ser., vol. 37. AGU, Washington, D.C., pp. 169–182.
England, P., Molnar, P., 2005. Late Quaternary to decadal velocity fields in Asia. J. Geophys. Res. 110 (B12401). doi:10.1029/2004JB003541.
Farr, T.G., Kobrick, M., 2000. Shuttle radar topography mission produces a wealth of data. Eos Trans. AGU 81 (48), 583–585.
Fialko, Y., Sandwell, D., Agnew, D., Simons, M., Shearer, P., Minster, B., 2002. Deformation on nearby faults induced by the 1999 Hector Mine earthquake. Science 297, 1858–1862.
Funning, G.J., Parsons, B., Wright, T.J., 2007. Fault slip in the 1997 Manyi, Tibet earthquake from linear elastic modelling of InSAR displacements. Geophys. J. Int. 169, 988–1008.
Gaudemer, Y., Tapponnier, P., Meyer, B., Peltzer, G., Guo, S., Chen, Z., Dai, H., Cifuentes, I., 1995. Partitioning of crustal slip between linked active faults in the eastern Qilian Shan, and evidence for a major seismic gap, the "Tianzhu gap", on the western Haiyuan fault, Gansu (China). Geophys. J. Int. 120, 599–645.
Gu, G., Lin, T., Shi, Z., 1989. Catalogue of Chinese Earthquakes (1831 BC–1969 AD). Science Press, Beijing.
Hanks, T.C., Kanamori, H., 1979. A moment magnitude scale. J. Geophys. Res. 84, 2348–2350.
Hanssen, R.F., 2001. Radar Interferometry, Data Interpretation and Error Analysis. Kluwer Academic Publishers.
Johanson, I.A., Bürgmann, R., 2005. Creep and quakes on the northern transition zone of the San Andreas fault from GPS and InSAR data. Geophys. Res. Lett. 32 (L14306). doi:10.1029/2005GL023150.
Lasserre, C., 2000. Fonctionnement sismique, cinématique et histoire géologique de la faille de haiyuan. Ph.D. thesis, Th`ese de doctorat, Université Paris 7.
Lasserre, C., Bukchin, B., Bernard, P., Tapponnier, P., Gaudemer, Y., Mostinsky, A., Dailu, R., 2001. Source parameters and tectonic origin of the 1996 June 1 Tianzhu (MW = 5.2) and 1995 July 21 Yongden (MW = 5.6) earthquakes near the Haiyuan fault (Gansu, China). Geophys. J. Int. 144 (1), 206–220.
Lasserre, C., Cavalié, O., Peltzer, G., Socquet, A., Doin, M.P., Sun, J., Xu, X., Shen, Z., Wang, Q., Gaudemer, Y., 2007. Interseismic Strain Across the Altyn Tagh and Haiyuan Faults at the Northern Edge of the Tibetan Plateau, Measured by Space Geodesy, Paper Presented at EGU General Assembly 2007, Vienna, Austria, 15–20 April 2007.
Lasserre, C., Gaudemer, Y., Tapponnier, P., Mériaux, A.S., der Woerd, J.V., Ryerson, F.J., Finkel, R.C., Caffee, M.W., 2002. Fast late Pleistocene slip rate on the Leng Long Ling segment of the Haiyuan Fault, Qinghai, China. J. Geophys. Res. 107 (B11). doi:10.1029/2000JB000060.
Lasserre, C., Morel, P.H., Gaudemer, Y., Tapponnier, P., Ryerson, F., King, G., Métivier, F., Kashgarian, M., Baichi, L., Taiyi, L., Daoyang, Y., 1999. Postglacial left slip-rate and past occurrence of M ≥ 8 earthquakes on the western Haiyuan fault, Gansu, China. J. Geophys. Res. 104, 17633–17651.
Lasserre, C., Peltzer, G., Crampé, F., Klinger, Y., der Woerd, J.V., Tapponnier, P., 2005. Coseismic deformation of the 2001 mw = 7.8 kokoxili earthquake in Tibet, measured by synthetic aperture radar interferometry. J. Geophys. Res. 110. doi:10.1029/2004JB003500.
Liu-Zeng, J., Klinger, Y., Xu, X., Lasserre, C., Chen, G., Chen, W., Tapponnier, P., Zhang, B., 2007. Millennium recurrence of large earthquakes on the Haiyuan fault near Songshan, Gansu province, China. Bull. Seismol. Soc. Am. 97 (1), 14–34. doi:10.1785/0120050118.
Massonnet, D., Feigl, K., 1998. Radar interferometry and its application to change in the earth's surface. Rev. Geophys. 36, 441–500.
Mériaux, A.S., Ryerson, F.J., Tapponnier, P., der Woerd, J.V., Finkel, R.C., Xu, X.W., Xu, Z.Q., Caffee, M.W., 2004. Rapid slip along the central Altyn Tagh Fault: morphochronologic evidence from Cherchen He and Sulamu Tagh. J. Geophys. Res. 109 (B06401). doi:10.1029/2003JB002558.
Mériaux, A.S., Tapponnier, P., Ryerson, F.J., Xu, X.W., King, G., der Woerd, J.V., Finkel, R.C., Li, H.B., Caffee, M.W., Xu, Z.Q., Chen, W.B., 2005. The Aksay segment of the northern Altyn Tagh fault: tectonic geomorphology, landscape evolution, and Holocene slip rate. J. Geophys. Res. 110 (B04404). doi:10.1029/2004JB003210.
Meyer, B., Tapponnier, P., Bourjot, L., Métivier, F., Gaudemer, Y., Peltzer, G., Guo, S., Chen, Z., 1998. Crustal thickening in Gansu-Qinghai, lithospheric mantle subduction, and oblique, strike-slip controlled growth of the Tibet Plateau. Geophys. J. Int. 135, 1–47.
Molnar, P., Tapponnier, P., 1975. Cenozoic tectonics of Asia: effects of a continental collision. Science 189, 419–426.
Nadeau, R.M., McEvilly, T.M., 2004. Periodic pulsing of characteristic microearthquake on the San Andreas fault. Science 303, 220–222.
Peltzer, G., Crampé, F., King, G., 1999. Evidence of nonlinear elasticity of the crust from the Mw = 7.6 Manyi (Tibet) earthquake. Science 286, 272–276.
Peltzer, G., Socquet, A., Lasserre, C., Mériaux, A., Tapponnier, P., Ryerson, R., 2006. InSAR observations of interseismic strain along the central Altyn Tagh fault consistent with Holocene slip-rate. EOS trans. AGU 87 (52) (Fall Meet. Suppl., Abstract T21E-02).
Puysségur, B., Michel, R., Avouac, J.P., 2007. Tropospheric phase delay in InSAR estimated from meteorological model and multispectral imagery. J. Geophys. Res. 111 (B12), 7166–7174.
Reinen, L.A., 2000. Slip styles in a spring-slider model with a laboratory-derived constitutive law for serpentinite. Geophys. Res. Lett. 27, 2037–2040.
Repetti, W.C., 1928. The epicenter of the Kansu earthquake of May 23, 1927. Bull. Seismol. Soc. Am. 18, 1–14.
Rosen, P.A., Hensley, S., Peltzer, G., Simons, M., 2004. Updated repeat orbit interferometry package released. Eos Trans. AGU 85 (5), 47.
Ryder, I., Bürgmann, R., submitted for publication. Spatial variations in creep rate on the central San Andreas Fault. Geophys. J. Int.
Ryder, I., Parsons, B., Wright, T.J., Funning, G.J., 2007. Post-seismic motion following the 1997 Manyi (Tibet) earthquake: InSAR observations and modelling. Geophys. J. Int. 169, 1009–1027.
Savage, J.C., Burford, R., 1973. Geodetic determination of relative determination plate motion in Central California. J. Geophys. Res. 78, 832–845.
Savage, J.C., Lisowski, M., 1993. Inferred depth of creep on the Hayward fault, Central California. J. Geophys. Res. 88, 787–793.
Scharroo, R., Visser, P.N.A.M., 1998. Precise orbit determination and gravity field improvement for the ERS satellites. J. Geophys. Res. 103 (C4), 8113–8127.
Schmidt, D.A., Bürgmann, R., Nadeau, R.M., d'Alessio, M., 2005. Distribution of aseismic slip rate on the Hayward fault inferred from seismic and geodetic data. J. Geophys. Res. 110. doi:10.1029/2004JB003397.
Scholz, C.H., Wyss, M., Smith, S.W., 1969. Seismic and aseismic slip on the San Andreas fault. J. Geophys. Res. 74, 2049–2069.
Shen, Z.-K., Wang, M., Li, Y., Jackson, D., Yian, A., Dong, D., Fang, P., 2001. Crustal deformation along the Altyn Tagh fault system, Western China, from GPS. J. Geophys. Res. 106 (B12), 30607–30622.
Tapponnier, P., Molnar, P., 1977. Active faulting and tectonics in China. J. Geophys. Res. 82, 2905–2930.
Tapponnier, P., Zhiquin, Xu, Roger, F., Meyer, B., Arnaud, N., Wittlinger, G., Jingsui, Yang, 2001. Oblique stepwise rise and growth of the Tibet Plateau. Science 294, 1671–1678.
Taylor, M., Peltzer, G., 2006. Current slip rates on conjugate strike-slip faults in central Tibet using synthetic aperture radar interferometry. J. Geophys. Res. 111 (B12). doi:10.1029/2005JB004014.
Uppala, S., Kållberg, P., Simmons, A., Andrae, U., 2005. The ERA-40 reanalysis. Q. J. R. Meteorol. Soc. 131, 2961–3012.
Van der Woerd, J., Ryerson, F., Tapponnier, P., Gaudemer, Y., Mériaux, A.-S., Caffee, M., Zhao, G., He, Q., 1997. Strain-styles, large-scale morphology and post-glacial slip-rates along the active Kunlun Fault (Qinghai,China). EOS Trans. 77 (46) (AGU Fall meeting Suppl).
Wang, Q., Zhang, P., Freymueller, J., Bilham, R., Larson, K., Lai, X., You, X., Niu, Z., Wu, J., Li, Y., Liu, J., Yang, Z., Chen, Q., 2001. Present-day deformation in China constrained by global positioning system measurements. Science 294, 574–575.
Wright, T., Parsons, B., Fielding, E., 2001. Measurement of interseismic strain accumulation across the North Anatolian Fault by satellite radar interferometry. Geophys. Res. Lett. 28 (10), 2117–2120.
Zebker, H.A., Rosen, P.A., Hensley, S., 1997. Atmospheric effects in interferometric synthetic aperture radar surface deformation and topographic maps. J. Geophys. Res. 102 (B4), 7547–7563.
Zhang, P., Molnar, P., Burchfiel, B.C., Royden, L.H., Wang, Y., Deng, Q., Song, F., Zhang, W., Jiao, D., 1988a. Bounds on the Holocene slip rate of the Haiyuan fault, north-central China. Quat. Res. 30, 151–164.
Zhang, P., Molnar, P., Zhang, W., Deng, Q., Wang, Y., Burchfiel, B.C., Song, F., Royden, L.H., Jiao, D., 1988b. Bounds on the average recurrence interval of major earthquakes along the Haiyuan fault in north-central China. Seismol. Res. Lett. 59, 81–89.
Zhang, W., Jiao, D., Zhang, P., Molnar, P., Burchfiel, B.C., Deng, Q., Wang, Y., Song, F., 1987. Displacement along the Haiyuan fault associated with the great 1920 Haiyuan, China, earthquake. Bull. Seismol. Soc. Am. 77, 117–131.
Zhang, P.-Z., Shen, Z., Wang, M., Gan, W., Bürgmann, R., Molnar, P., Wang, Q., Niu, Z., Sun, J., Wu, J., Hanrong, S., Xinzhao, Y., 2004. Continuous deformation of the Tibetan Plateau from global positioning system data. Geology 32, 809–812.